2021-01-0405 Published 06 Apr 2021

Multi-Dimensional Spark Ignition Model with Distributed Energy Input and Integrated Circuit Model

Kyeongmin Kim, Corey Tambasco, Matthew Hall, and Ron Matthews University of Texas at Austin

Sachin Joshi, Douglas L. Sprunger, and Daniel O'Connor Cummins Inc

Citation: Kim, K., Tambasco, C., Hall, M., Matthews, R. et al., "Multi-Dimensional Spark Ignition Model with Distributed Energy Input and Integrated Circuit Model," SAE Technical Paper 2021-01-0405, 2021, doi:10.4271/2021-01-0405.

Abstract

A multi-dimensional model of the spark ignition process for SI engines was developed as a user defined function (UDF) integrated into the commercial engine simulation software CONVERGE™ CFD. For the present research, the model simulated spark plasma development in an inert flow environment without combustion. The UT model results were then compared with experiments. The UT CONVERGE CFD-based model includes an electrical circuit sub-model that couples the primary and secondary sides of an inductive ignition system to predict arc voltage and current, from which the transient delivered electrical energy to the gap can be determined. Experimentally measured values of the arc resistance and spark plug calorimeter measurements of the efficiency of electrical to thermal energy conversion in the gap were used to determine the thermal energy delivered to the gas in the spark gap for different pressures and gap distances. A novel feature of the presented model is that the thermal energy delivered to the gap is distributed uniformly along the arc rather than at discrete points along the arc. This feature was found to greatly reduce the tendency of the arc to distort its shape and tangle itself in a non-physical way, as is the tendency when discrete energy input locations are used. It was found that the tangled distortion of the arc when using discrete energy input was due to perturbations along the arc caused by differential expansion of the gas along groups of adjacent mesh cells that either had energy input or did not. The distributed energy feature also gave arc temperature distributions that were more spatially uniform and had steeper temperature gradients, consistent with experimental arc images. Testing of the model included simulations of arc movement in the presence of a crossflow of nitrogen through the gap. These results were compared with experimental high-speed video images of arc movement for a spark plug of similar geometry and taken over a range of pressures and crossflow velocities in a high-pressure constant volume vessel. There was good agreement between the simulations and experimental images, including the observed off-axis movement of the arc in response to a recirculation zone developed downstream from the ground electrode (anode).

Introduction

The energy from the ignition system is a key element that determines the nature or the plasma column within the spark plug gap and determines the success of the ignition and combustion of the fuel-air mixture in a spark ignition engine. A sufficiently high voltage across the spark plug gap must be applied by the ignition system to breakdown the fuel-air mixture within the spark plug gap. The plasma column formed after the breakdown is where the energy from the ignition system is delivered to the gas inside the cylinder. The amount and duration of the thermal energy delivered must be sufficient to ignite the fuel-air mixture and sustain the flame kernel until the chemical heat release from the combustion can create a self-sustaining turbulent flame. Successful ignition depends on many factors including electrical components in the ignition circuit, fuel type, fuel-air mixture ratio, mixture homogeneity, dilution, residual fraction, in-cylinder bulk flows and turbulence, spark plug geometry, spark timing and duration, and the characteristics of the electrical energy delivery. Recent stringent emissions standards have led to high dilution rates and lean mixture operation of spark ignition engines, which can create challenging conditions for reliable ignition and combustion with minimum cycle-to-cycle variation.

Detailed ignition sub-models can be integrated with computational fluid dynamics (CFD) software such as CONVERGE™ CFD, to simulate the ignition process. Many researchers have investigated and modeled spark channel behavior within the local flow and its effects on the flame kernel development. Fan et al. introduced a Discrete Particle Ignition Kernel (DPIK) model where the flame kernel is assumed to be spherical and is described using discrete particle markers [1]. This Lagrangian particle approach made it less sensitive to numerical mesh size. Duclos et al. proposed an Arc and Kernel Tracking Ignition Model (AKTIM) for describing the flame kernel expansion [2]. The spark is

modeled by a set of particles along the spark path that can be elongated by the mean flow field. Their model also includes the secondary side of the electrical inductive ignition system. Each particle receives energy from the ignition circuit. Dahms et al. developed a Spark Channel Ignition Monitoring Model (SparkCIMM) which models the spark channel with discrete particles [3]. These particles can also be stretched by the local flow. Restrike of the stretched spark channel is modeled in SparkCIMM by resetting the spark marker particles to their original location when the spark channel exceeds a predefined length. The spark energy deposition rate was assumed to be uniform along the spark channel and constant in time. Lucchini et al. introduced a comprehensive model for ignition and flame kernel development [4]. The spark channel was modeled with discrete particles which receive energy from a simplified ignition circuit model. Restrike of the stretched spark channel was modeled with two different criteria, column voltage and the maximum channel length. Numerical studies using an Energy Deposition Model were conducted recently to simulate the spark ignition process in an engine [5,6]. Energy is deposited into a spherical energy source with the energy deposition rate determined from the measured voltage and current. Scarcelli et al. showed that the Lagrangian-Eulerian Spark-Ignition (LESI) model is in good agreement with visualized experiments at non-quiescent, engine-like conditions [7]. However, short-circuit and restrike behavior were not included in this model. Sforza et al. [8] used Lucchini's model to investigate the flame kernel development and flame stretch in combustible gas mixtures. Lucchini's model includes a simplified circuit model with a secondary circuit and flame kernel model with discrete particles. We extended the ignition circuit model including the primary circuit and solving the differential electrical equations that govern the circuit behavior. Also, the energy deposition is continuous along the spark channel. Masuda et al. [9] developed a model of restrike and short-circuit behavior based on the voltage across the spark channel. They used the ignition circuit model proposed by Duclos et al. [2], which is a secondary side of the electrical inductive ignition system. Their restrike and short-circuit model is similar to our model, but they still use discrete particles for the energy deposition.

There have been several studies related to the flow around the spark plug gap and the effect of the local flow on the spark kernel movement and flame kernel formation. Mantel found that the orientation of the spark plug relative to the mean flow changes the mean flow field around the spark plug gap and heat transfer to the electrode [10]. These are important factors in the development of the initial flame. Kim and Anderson investigated the method to determine the gas velocity near the spark plug gap using voltage and current profiles, known as spark anemometry [11]. Gardiner et al. showed improvements of spark anemometry using a constant current spark and high-speed video [12]. From the high-speed video, they found that the velocity of the spark head is about one-half of the freestream velocity. This velocity difference between the spark gap velocity and the freestream velocity was also reported by Kim and Anderson.

Inductive ignition systems have been studied by many researchers to understand their behavior. Stevenson et al. studied comprehensive modeling of an automotive ignition system, including the ignition circuit and ignition coil [13]. They simulated the transient behavior of the current and voltage during charging and discharging with a simplified model. They also modeled the ignition coil using finite element analysis (FEA) calculations to better represent the inductance, capacitance, and resistance of the ignition coil. Wang et al. developed an ignition circuit model using Laplace transforms. Parasitic parameters of the spark plug were extracted with finite element methods [14]. Yu et al. investigated the effect of circuit parameters on spark discharges and spark energy properties [15]. A simplified electrical circuit model was verified using experimental results. They found that the decrease of secondary circuit resistance, the increase of spark plug gap, the increase of the ignition coil coupling coefficient, and the increase of the ignition coil inductance ratio produce higher spark energy. Tan el al. modeled the inductive ignition circuit using Laplace transforms and compared their results with experiments [16]. Most of the studies involved evaluating the voltage and current response from the ignition circuit alone or simulating the time-resolved response of the ignition circuit. As an alternative, the transient behavior of the ignition circuit can be studied with a circuit model added to the CFD software to accurately simulate the ignition system and flow field simultaneously, as is done here. To the authors' knowledge, this type of integrated ignition model has not been presented previously in the literature.

Spark plug calorimeters have been used to evaluate the thermal energy deposited into the gas by many researchers. Roth et al. first introduced the measurement of spark energy delivered to the gas with both constant-volume and constant-pressure calorimeters [17]. They performed a fundamental study of the effects of the electrode diameter, gap distance, and thermal diffusivity of the gas on the electrical-to-thermal energy conversion efficiency with monatomic gases. Merritt was first to create a spark calorimeter consisting of two chambers and a differential pressure transducer [18]. Franke and Reinmann used a spark calorimeter with this differential pressure sensing concept [19]. They measured the energy delivered to the gas comparing five different ignition systems that included both capacitive and inductive ignition type at pressures up to 16 bar. Teets and Sell used a spark calorimeter to study the thermal energy deposition characteristic of three different ignition systems that included an inductive system, a plasma jet ignitor, and an ultra-short pulse ignitor [20]. Abidin et al. investigated the effect of dwell time, gap distance, and pressure on the breakdown voltage and the electrical-to-thermal energy conversion efficiency [21]. Alger et al. used a spark calorimeter to measure the energy delivered to the gas while investigating the effect of spark plug design on the initial flame kernel development [22].

Ignition Circuit Model

Figure 1(a). shows the ignition circuit used in the model presented here. Figure 1(b) shows the location of voltage and current used in the model. The circuit is representative of current inductive-type ignition systems and includes both the primary and secondary sides of the ignition coil. Capacitor

FIGURE 1 (a) Schematic of ignition circuit model; (b) voltage and current labeling in the model.

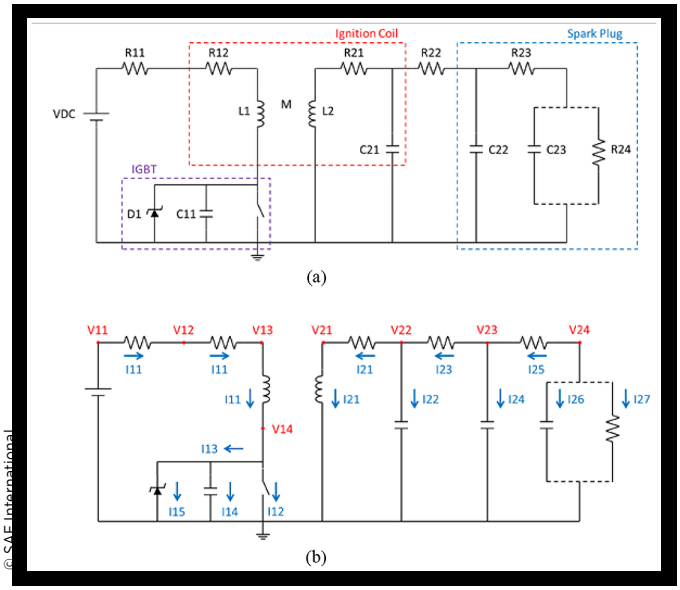

C21 is the parasitic capacitance of the secondary winding. R12 and R21 represent the resistance of the primary and the secondary windings, respectively. The violet boxed part is the simplified model of the insulated-gate bipolar transistor (IGBT), which acts as the switch of the ignition circuit. R22 is the resistance of the high-tension lead and C22 and C23 represent the parasitic capacitances of the spark plug separated by the spark plug resistance R23. Spark column resistance R24 replaces the capacitance C23 following breakdown during the discharge. After the end of the discharge, R24 is removed and again replaced by C23.

The resistances of the wires, ignition coil, and spark plug were measured with an ohm meter. Additionally, the current dependent spark plug resistance was measured by short-circuiting the two electrodes and measuring the voltage drop across the spark plug and the current for a coil discharge. The inductances of the primary and secondary windings were calculated from the measured voltage and current profile with a Zener diode replacing the spark plug to give a constant voltage following breakdown. The governing equations are:

$$V_{11} - R_{11}I_{11} - R_{12}I_{11} - L_1\frac{dI_{11}}{dt} - M\frac{dI_{21}}{dt} - V_{14} = 0 \qquad (1)$$

$$V_{24} - R_{23}I_{25} - R_{22}I_{23} - R_{21}I_{21} - L_2\frac{dI_{21}}{dt} - M\frac{dI_{11}}{dt} = 0 \qquad (2)$$

The ignition circuit model was developed by solving differential equations (1, 2) for the primary and secondary circuit. With the DC power voltage and dwell time for building an electromagnetic field in the coil given, the transient response of the ignition circuit model can be simulated. When the voltage across the capacitance C23 exceeds the breakdown voltage (given by either a separate breakdown voltage model or as was done here with a user input), the spark column resistance R24 replaces the capacitance C23 to simulate the spark column between the two electrodes. Electrical power input to the spark plug gap is calculated by multiplying the voltage and current across the spark column resistance R24. However, this electrical energy input is not the energy deposited into the gas between the spark gap. The thermal energy input is calculated using the electrical-to-thermal energy conversion efficiency. This conversion efficiency is an experimental value determined through calorimeter measurements and is an input to the model. After the end of the discharge, when the secondary current decreases to zero, spark plug capacitance C23 replaces the spark column resistance R24. The developed MATLAB version of the ignition circuit model was validated with experimental results and PSpice simulations. PSpice is a commercial electronic circuit simulation software from OrCAD. The ignition circuit model was then integrated into CONVERGE CFD in the form or a UDF (User Defined Function) to simulate the ignition circuit and the flow field simultaneously.

Within the newly developed ignition UDF, modifications were made to the default CONVERGE CFD source model which simulated the spark column between the gap. In the default CONVERGE CFD ignition model, a group of points is used to model the spark column and these ignition points move with the flow between the spark gap. The energy is deposited into the cells where these points are located. However, when the number of points is not sufficiently high compared to the number of cells along the modeled spark column, the energy is only deposited at discrete points along the spark column. In addition, the point source is infinitesimal and the energy for that region of the spark is only deposited into the one cell where the point exists. The local pressure and temperature change in the cell with the energy input and is affected by the size of the cell. Lastly, this point source method of energy delivery cannot account for the effect of column diameter. Some of these effects can be seen in Figure 2(a).

Our research team developed a distributed energy input model for the spark column to resolve the issues discussed above. In this model, the spark column is modeled as a series of cylinders as shown in Figure 2(b). The diameter of the cylinder represents the diameter of the spark column. Because the energy is deposited into the volume of the cells occupied by the cylinder, the discrete energy input and spark diameter issues are resolved. In addition, the distributed energy input model minimizes the effects of grid resolution around the spark column. CONVERGE CFD also has an option for a cylindrical ignition source, however, only one cylinder can be used as this cylindrical source and the movement of the cylinder is limited to translation without rotation. Therefore,

FIGURE 2 Comparison of energy input model (a) discrete energy input and (b) distributed energy input.

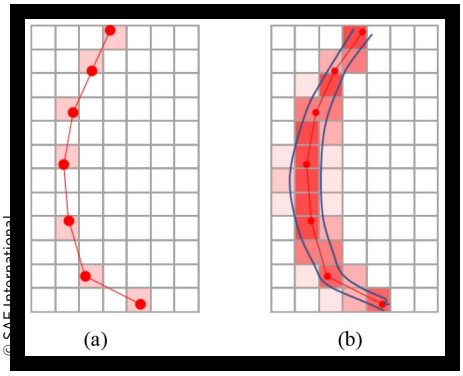

the CONVERGE CFD cylindrical source model can only be used to model a stationary spark column. In the new distributed energy input model developed and used for the present paper, CONVERGE CFD identifies the centers of the top and bottom surfaces of the cylinder as a point source. This ensures that these points can move with the flow. Reconstructing the cylindrical shape from these moving points can better model the actual spark column movement with distributed energy input.

Stretching of the spark column due to crossflow increases the voltage across the gap. If the voltage between any two points along the spark column is high enough to create a new spark column between those points, a short-circuit or re-strike occurs between those two points creating a shorter path for the current flow. To model this phenomenon, the voltage between any two points along the spark column is calculated based on the gap voltage and the total column length, with the assumption that the voltage difference is linear with the column length as given in eqn. 3.

$$V_{AB} = \frac{V_{gap}}{l_{total}} \times l_{AB} \tag{3}$$

where V_{AB} is the voltage between points A and B in the spark column, V_{gap} is the gap voltage, l_{total} is the total column length, and l_{AB} is the length between points A and B. The voltage needed to create a new spark path can be calculated from the breakdown voltage, the gap distance, and the distance between two points. From Paschen's law [23], the breakdown voltage is taken to be linear with the gap distance. The voltage to create the short-circuit or re-strike was calculated using eqn. 4.

$$V_{SC} = \frac{V_{BD}}{d_{gap}} \times d_{SC} \times C \tag{4}$$

where V_{SC} is the short-circuit or re-strike voltage to create a new path, V_{BD} is the initial breakdown voltage, d_{gap} is the spark gap distance, and d_{SC} is the distance between points A and B in the spark column. A constant C is used to correlate the calculated voltage with the measured voltage from the experiments. If V_{SC} is higher than V_{AB} for any given two points along the spark column, a new cylindrical column model is created between those points as seen in Figure 3.

One possible practical limitation to the general use of a model such as this, having an integrated circuit model, is that it requires knowledge of the values of the circuit element parameters, something that is not always known by the user.

FIGURE 3 Restrike model for the stretched spark column.

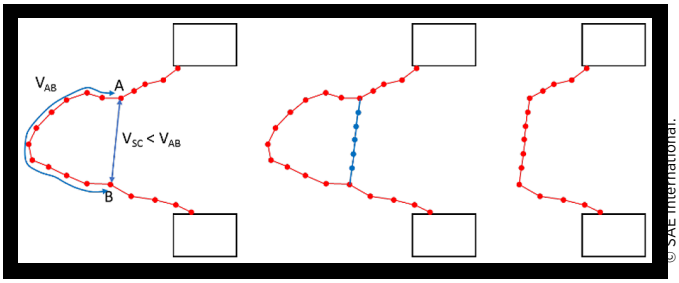

Calorimeter

Experimental calorimeter measurements were made to determine the conversion efficiency of the electrical energy delivered to the spark gap to thermal energy deposited in the gas. This was a model input that varied with both pressure and gap distance. A photo of the calorimeter is shown in Fig. 4(a), along with a cross-sectional drawing in Figure 4(b). The calorimeter was machined from stainless steel in two pieces and designed to accommodate a 14 mm spark plug. It had two chambers, a small cylindrical chamber into which the spark plug was inserted and a second, reference pressure chamber in which the chip-based pressure sensor was located. The advantage of this more complicated design over more conventional spark calorimeters is that it measures the very small differential change in pressure associated with energy

FIGURE 4 (a) Photo of spark calorimeter; (b) section drawing of the calorimeter.

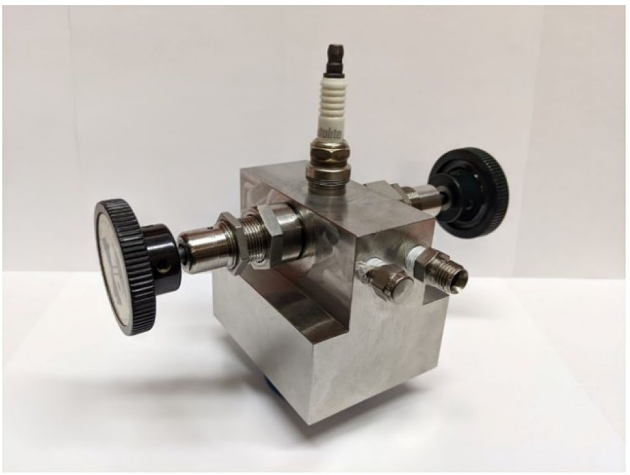

(a)

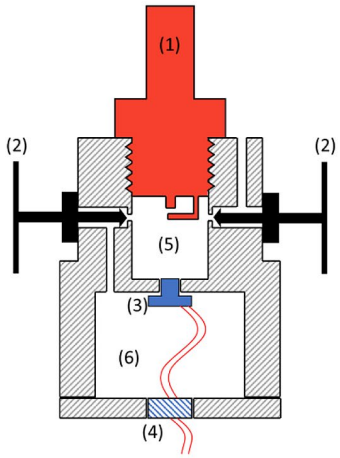

1. Spark plug
2. Valves
3. Differential pressure transducer
4. High pressure electrical feedthrough
5. Main chamber
6. Reference chamber

(b)

FIGURE 5 Schematic of calorimeter setup.

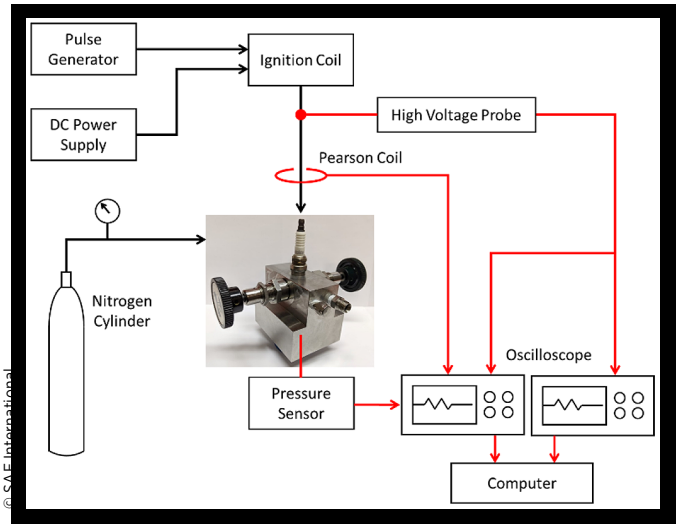

deposition from the arc to the gas relative the high initial pressure; this increases the dynamic range and sensitivity of the pressure measurement. Details of the calorimeter design and operation can be found in reference [24].

Figure 5 shows a schematic of the calorimeter experimental setup. Nitrogen was used to pressurize the calorimeter to the desired level. This pressure was measured using precision Bourdon tube pressure gauges. Time-resolved measurements of spark plug voltage and current were made to determine the electrical energy delivered to the spark plug. A Tektronix Model P6015A high voltage probe measured the breakdown and follow-on voltages at the top of the spark plug. The current-dependent resistance of each spark plug was measured and the voltage drop across the internal resistance was subtracted from the voltage measured at the top of the plug to obtain the gap voltage. A Pearson Model 110 current sensor was used to measure the discharge current. The voltage, current, and pressure sensor signals were recorded using a 100 MHz 4-channel Tektronix oscilloscope. Breakdown voltages were recorded separately since a faster time-base setting was needed to resolve these very short duration events.

High-Pressure Optical Vessel

A constant volume high-pressure vessel with optical windows was used to visualize the spark column event with a high-speed camera. The combustion vessel was cylindrical in shape and had an inside diameter of 7.9 cm and height of 1.4 cm. The spark plug was located at the center of one of the disk-shaped sidewalls. Quartz windows allowed optical access to the spark plug. The nitrogen flow from the high-pressure cylinder was introduced to the spark plug gap in the combustion vessel by a copper tube. The pressure regulator and a relief valve at the outlet of the vessel controlled the pressure inside the vessel and the gas flow rate. The flow rate was measured with a rotameter located downstream from the relief valve. The rotameter was calibrated with a diaphragm-type gas meter. The free flow velocity out of the gas supply tube was calculated based on the measured flow rate and the diameter of the tube.

Visualization of spark column stretch under crossflow was done using a Photron Fastcam Mini high-speed camera. The optical path of the camera was set to capture the side view of the spark plug gap. The ground electrode of the spark plug was directed perpendicular to the crossflow. The frame rate of the camera was set to 50,000 frames per second (FPS) to capture the milliseconds-order spark event. An light source was used to capture the outline of the spark plug and electrode.

FIGURE 6 Schematic of the high-speed camera setup.

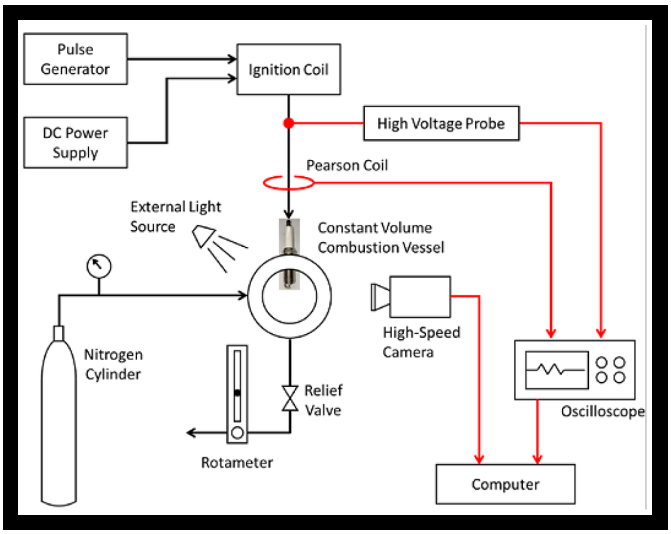

All of the measurements were made using a 14 mm spark plug designed for natural gas engines. The spark plug had a J-type ground electrode with 2 mm width and stepped center electrode with 0.6 mm and 2 mm diameters. The dwell time used was 4 ms. Nitrogen was used for all of the measurements of spark column behavior.

Calorimeter Results

Table 1 shows a few of the circuit parameters used in the ignition circuit model and the units for those parameters. The model incorporated the same parameter values as the coil used for the experiments. The coil was a pre-production prototype so most of the inductance and resistance values are considered proprietary, and are therefore, not shown.

Calorimeter measurements were made at 12 bar pressure to compare with the simulation results without crossflow. Figure 7 shows the primary current profiles during the charging process for both the experiment and simulation. At the time of the ignition signal, -4 ms, the primary current starts to increases and charges the ignition coil during the 4 ms dwell time.

After the 4 ms dwell time, the IGBT was switched off and the magnetic field around the primary and secondary coils

TABLE 1 Parameter for the ignition circuit model.

DC supply voltage	13.5 V
Primary wire resistance, R11	NA Ω
Primary winding resistance, R12	NA Ω
Primary Inductance, L1	NA mH
Primacy circuit capacitance, C11	NA pF
Zener voltage	NA V
Secondary inductance, L2	NA H
Coefficient of mutual inductance, kM	NA
Mutual inductance, M	$k_M\sqrt{L_1L_2}$
Secondary circuit capacitances, C21	NA pF
Spark plug capacitances, C22, C23	20 pF
Secondary winding resistance, R21	NA Ω Se
Secondary wire resistance, R22	Ω
Spark plug internal resistance, R23	4000 Ω

collapsed. Current and voltage profiles during this time period are shown in Figures 8 to 10. The downward transition at the end of the 4 ms long TTL signal triggered the ignition coil at 0 sec. In the experiments, however, the current and voltage profiles start to change after 12 µs. The origin of the 12 µs delay in the case of the experiments is thought to be mostly attributable to the known switching time of the IGBT of 11.5 µs [25]. We use a simplified model of the IGBT and hence do not predict the observed 12 µs delay. Therefore, the Figures 8, 9, and 10 show that the simulated curves are displaced 12 µs with respect to the experimental measurements. The primary current becomes zero in 6 µs and shows some oscillation due to the effects of capacitance. During this 6 µs period, the secondary current increases from zero to

40 mA. This secondary current was measured at the top of the spark plug and corresponds to the current flowing

FIGURE 7 Primary current profile during charging.

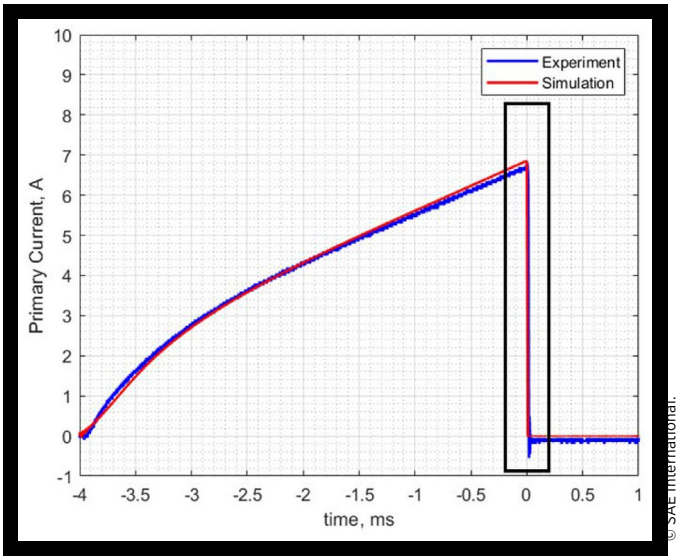

FIGURE 8 Primary current at the end of the dwell time (close-up of black box in Figure 7).

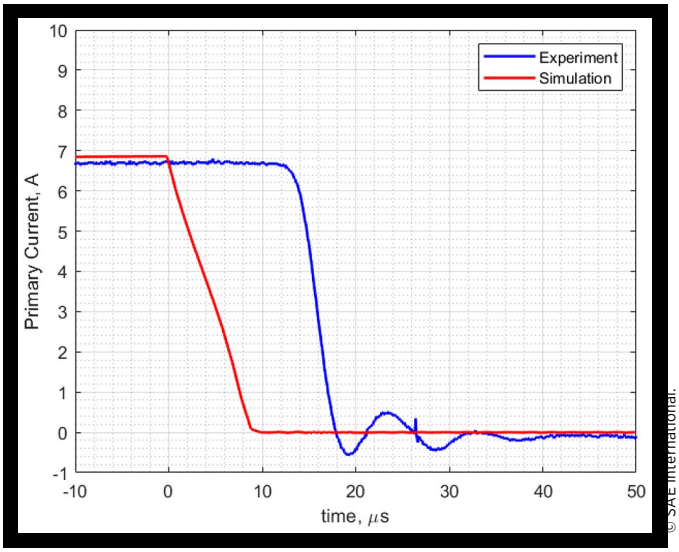

FIGURE 9 Secondary current profile at the end of the dwell time.

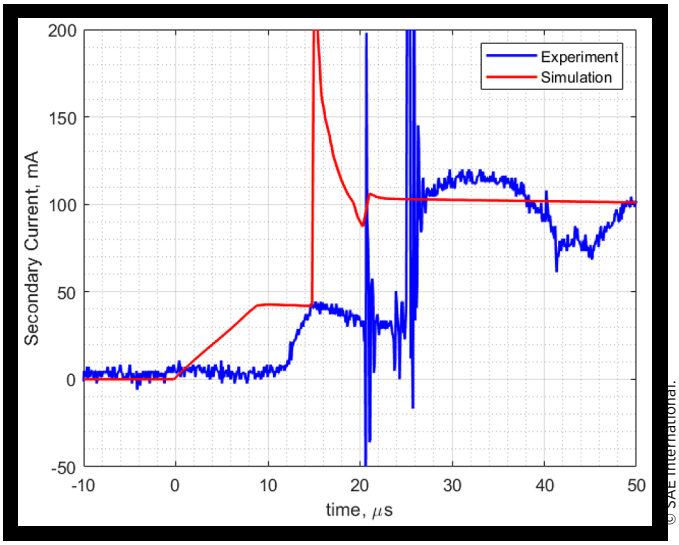

through the secondary wire resistance R22 in Figure 2. After this 6 µs period, the measured secondary current stays relatively constant, making the voltage difference across the high-tension wire resistance R22 constant. The simulation results showed that the secondary current flowing through the secondary inductance L2 kept increasing after this 6 µs period until breakdown at 25 µs, This current, however, could not be measured experimentally. The difference between the current through the secondary inductance and through the wire resistance up until the time of breakdown flowed through the capacitances in the secondary circuit, building-up the voltages across the capacitances. This voltage build-up is shown in Figure 10. At 12 bar pressure, the breakdown occurs at 11.6 kV. This breakdown voltage was a user input in the ignition circuit model; we are developing a breakdown voltage model that is intended to be superior to Paschen's law. The time from the start of the decrease of the primary current to

FIGURE 10 Secondary voltage profile at the end of the dwell time.

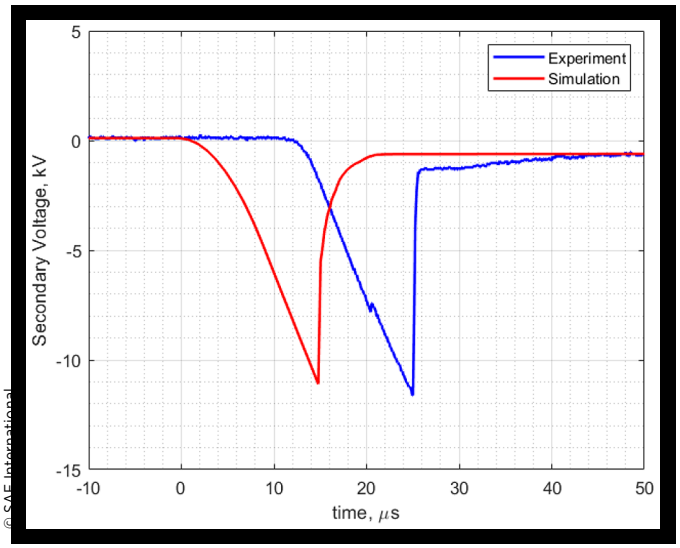

breakdown was about 12 μs for both the experiment and simulation.

Figure 11 shows the secondary voltage and current during the discharge. Figure 11(a) is measured voltage at the top of the spark plug. Figure 11(b) is the voltage trace after subtracting the voltage drop across the internal resistor, and thus, represents the gap voltage. The gap resistance calculated from the measured gap voltage and current is shown in Figure 12 as a function of current. The curve fit of the gap resistance (the red trace) is used in the ignition circuit model as R24 to simulate the discharge process. The secondary voltage varied between 300 and 500 V for both the experiment and the simulation. The discharge duration was about the same for each at 4.5 ms. The secondary current decreases linearly from 100 mA to zero. The electrical energy deposited into the gap as measured from the gap voltage and the current was 39.95 mJ.

Figure 13 shows an example of a recorded pressure trace from the calorimeter along with the voltage profile. As seen in Figure 13, there is a periodic ringing superimposed upon the pressure signal. It was found that the observed fluctuations appear to be an artifact due to Helmholtz resonator behavior of the sensor [24].

$$E_{therm} = \frac{V}{\gamma - 1}\Delta P \tag{5}$$

From the pressure rise and the volume of the calorimeter using eqn. 5 [21], the total thermal energy input was found to be 5.89 mJ. and the calculated electrical-to-thermal energy conversion efficiency was 14.7 %. This conversion efficiency was used in the ignition circuit model to convert the electrical energy input to the thermal energy input. The actual electrical-to-thermal energy conversion efficiency varies during the discharge period depending on the type of discharge, breakdown, arc, or glow. The electrical-to-thermal energy conversion efficiency of 14.7% used in the model was derived from the calorimeter experiments where the gas was quiescent. It should be noted that this likely resulted in an under-prediction of the actual conversion efficiency once the arc left the vicinity of the gap. This represents an uncertainty in the model that should be studied and addressed with future development of the model.

FIGURE 11 Profiles during discharging, (a) measured voltage, (b) gap voltage, and (c) secondary current.

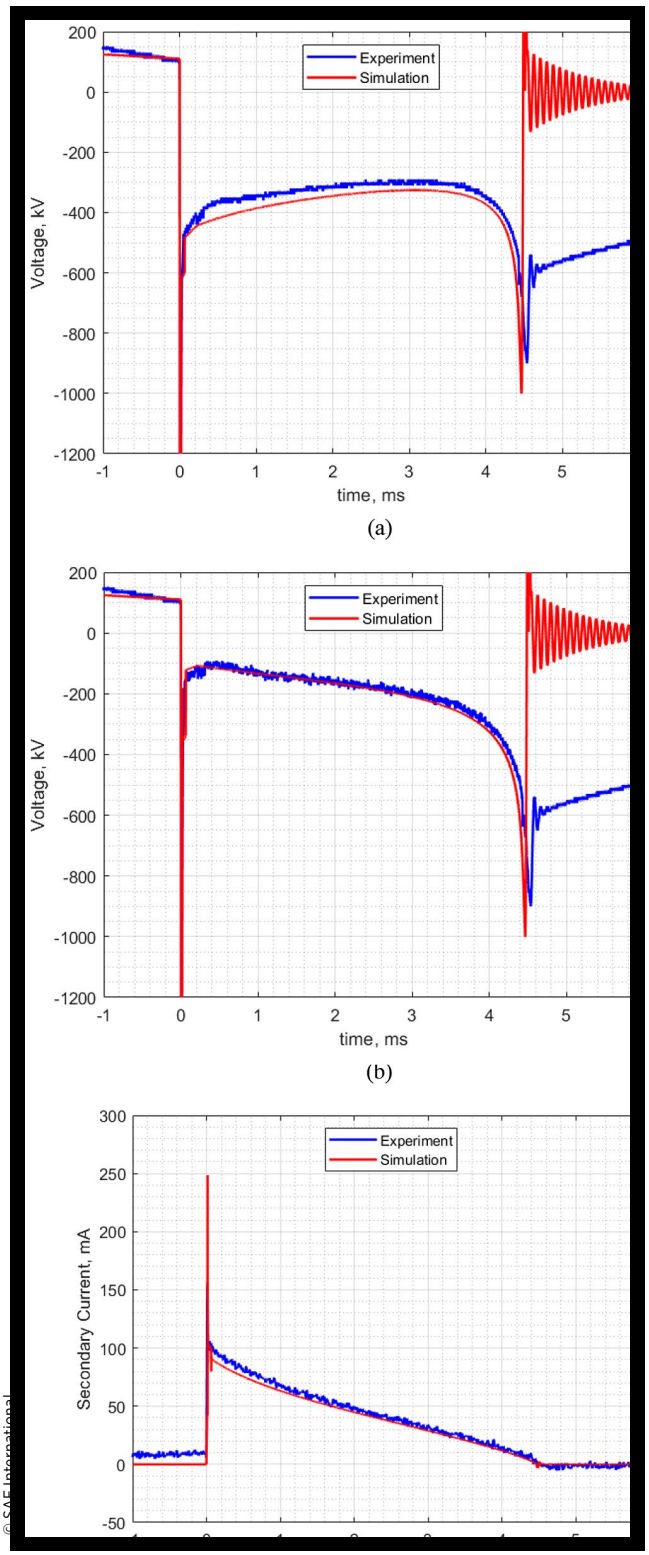

FIGURE 12 Calculated gap resistance and curve fit vs. current.

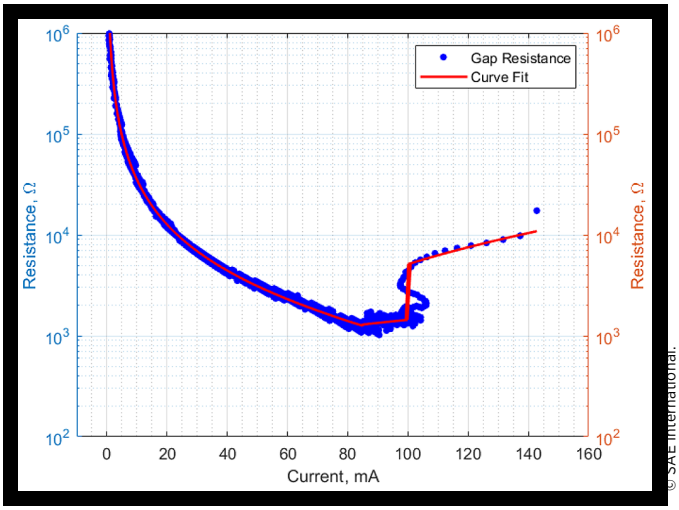

FIGURE 13 Pressure rise vs. time.

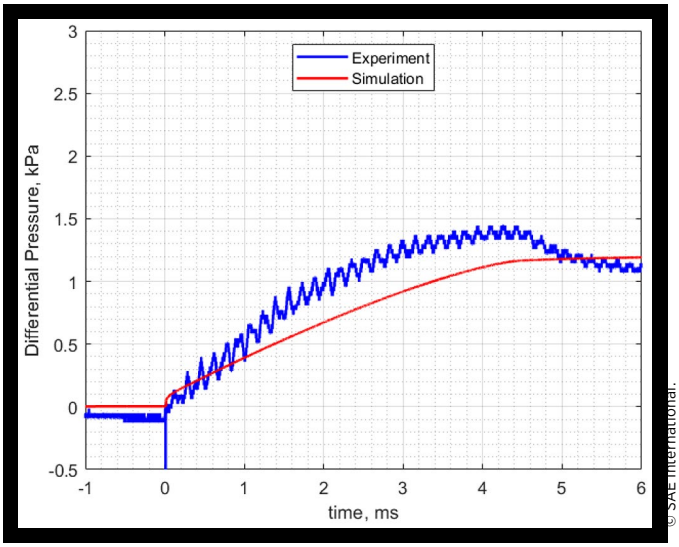

The pressure sensor used in the experiment was not fast enough to give a separate energy conversion efficiency for the breakdown process. Figure 13(b) shows the pressure rise from the simulation. In this simulation, the temperature boundary conditions on the spark plug electrodes and calorimeter wall were set to adiabatic. Any heat losses between the spark column and the surfaces are included in the electrical-to-thermal energy conversion efficiency. The pressure rise was about 1.4 kPa from the experiment. However, the simulation showed the pressure rise to be approximately 1.2 kPa. Considering that the voltage and current behavior during the discharge is well demonstrated by the simulation, a difference in the shape of the pressure rise might be associated with the energy deposition during the breakdown. The breakdown occurs over a very short time scale, on the order of nanoseconds, and the energy conversion efficiency is very high (~90%) [26]. The equipment used in the experiment was not fast enough to capture the voltage and current changes within this short time period. The under-prediction of the maximum pressure rise could possibly be associated with uncertainty in the actual gap voltage, determined by subtracting the spark plug internal resistance from the measured secondary voltage.

Energy Input Model

A CONVERGE™ CFD simulation at 12 bar pressure and 5 m/s free stream velocity was carried out to compare the discrete energy input and the distributed energy input models in the presence of crossflow. As the discrete energy input could be done simultaneously with the ignition circuit model, a constant power input of 3 W was used for both simulations. The 3 W power input with a 2 ms duration gives 6 mJ of thermal energy, which is comparable to the result from the calorimeter measurement. Figure 14 shows individual examples of gap voltages from the combustion vessel measurement with different levels of crossflow velocity. The large fluctuations are associated with restrike events, which become more frequent as velocity increases. The discharge duration decreased from 4.5 ms to 1.8 ms with a crossflow velocity of 5 m/s.

Part of the actual combustion vessel is used as the simulation domain to save time and computational resources. The boundary of the simulation domain was set to where the jet flow from the tube does not affect the local flow. The base mesh size was 0.4 mm for the entire simulation domain. Three levels of fixed embedding were applied for the flow out of the tube and for the possible locations of the spark channel around the spark plug gap. Thus, the minimum mesh size was 50 μm. The RNG k-ε turbulence model was used to predict the flow field around the spark plug.

Figure 15 shows the temperature contours for the discrete points energy input simulation. The black line is the location of the column model connecting the 40 points where the energy is deposited. The energy is deposited into the cell where each point is located. As the points are moved by the crossflow from the initial straight line spanning the gap, the distance

FIGURE 14 Gap voltages with crossflow at a pressure of 20 bar and gap of 0.66 mm.

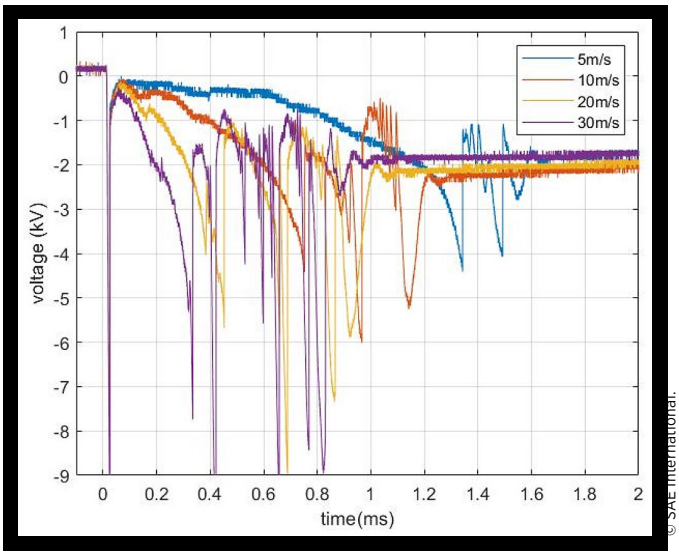

between the adjacent points becomes longer. This makes the cells where the energy is deposited isolated from the surrounding cells. Only one cell gets energy deposition and the other cells around it get zero energy deposition. This discontinuous energy deposition perturbs the local flow field and thus the local flow diverges from the discrete points. This results in irregular movement of the spark column, which can be seen from Figure 15.

Figure 16 shows the simulation results for our new distributed energy input model. The same 40 points as for the discrete energy input model were used. These points start and end at the center points of the top and bottom surfaces of the cylindrical spark column model. Thus, 39 cylinders form the spark column in this distributed energy input simulation. The energy is deposited into all of the cells occupying the volume of the 39 cylinders. This makes the energy deposition more

FIGURE 15 Simulation results of the discrete points energy input ignition model.

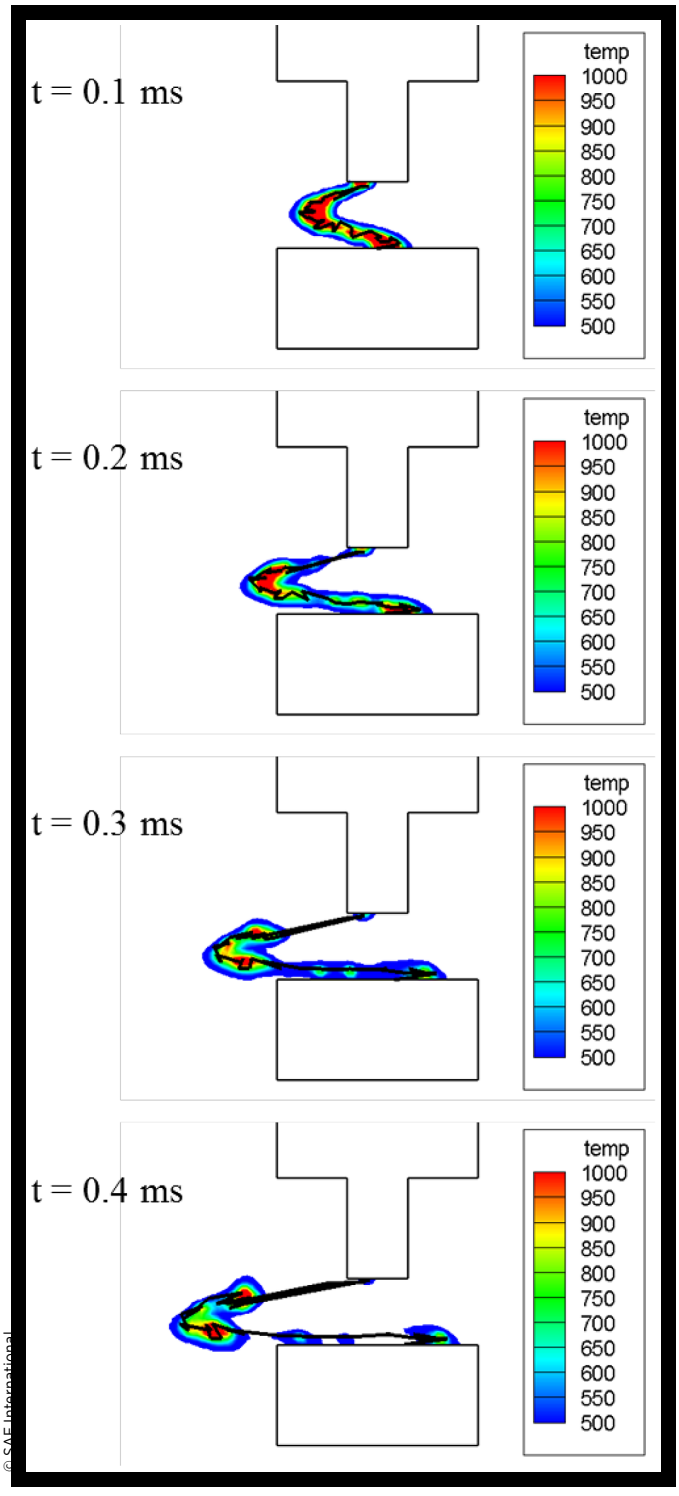

FIGURE 16 Simulation results with our new distributed energy input ignition model.

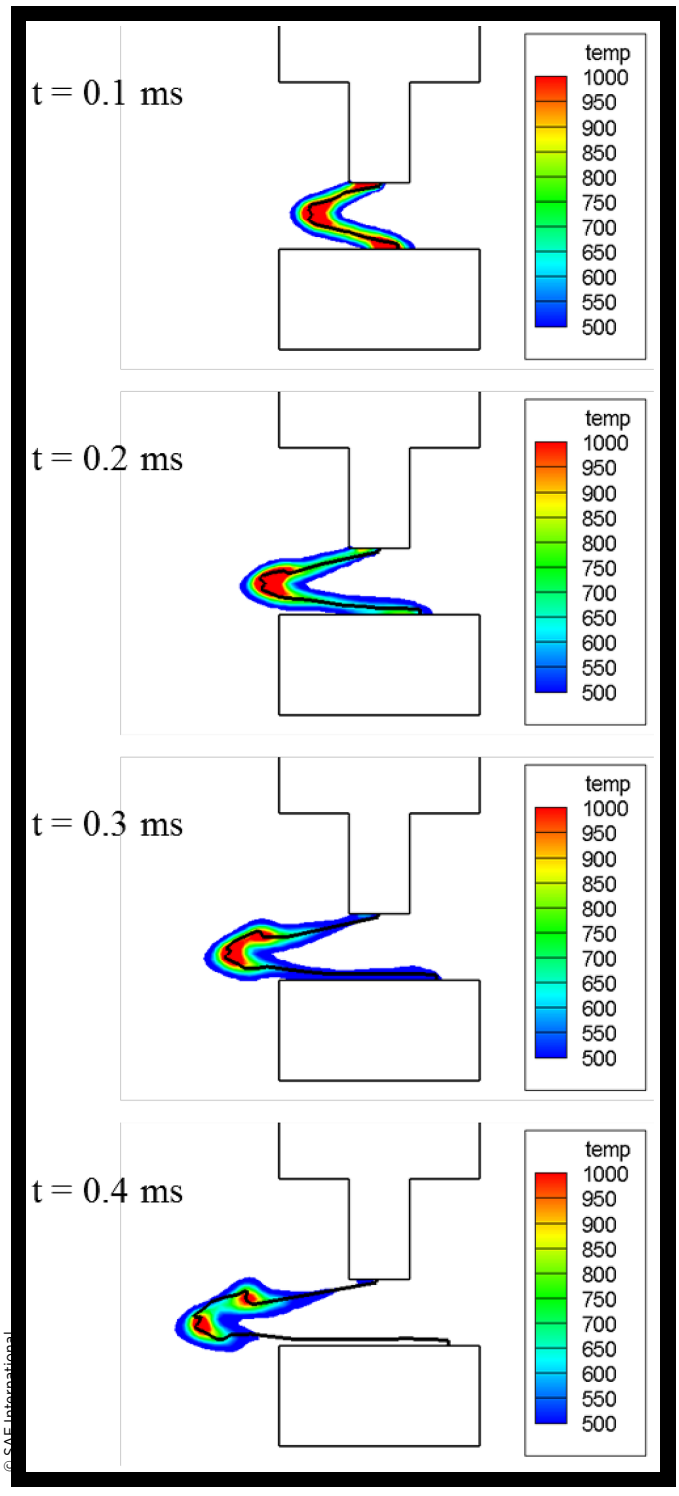

realistic compared to the discrete energy input. Also, we can account for the diameter of the spark column with our new model. In this simulation the spark column diameter was set to 0.2 mm. The minimum cell size around the spark gap is 50 µm. Therefore, the cross section of the spark column occupies 16-20 cells depending on the orientation.

The ignition plasma in the simulations is modeled through the thermodynamic properties of the working fluid. Temperature and pressure are determined by the specific heats, and thermal diffusivities of the species in the cell. These determine radial temperature distributions and current densities in the arc. This is in response to the energy input as it is distributed among the mesh cells that are defined by the location of the arc. The arc position is then a function of the movement of the gas in the spark gap.

The base grid size in the simulation domain was 0.4 mm and three levels of fixed embedding was used around the spark plug gap. Therefore, the minimum mesh size around the spark plug gap was 50 µm. Fixed embedding rather than adaptive mesh refinement provided better load balance for parallel computation. A coarser grid may not properly resolve the flow field around the spark plug gap, which is an important factor for the spark channel elongation. Some levels of mesh refinement are desired to better predict the flow field and spark movement.

The total length of the spark channel varied from 0.6 mm for the unstretched spark to 5-6 mm for fully stretched spark. Again, the minimum mesh size used in the calculation around the spark plug gap was 50 µm. Therefore, the spark channel occupied roughly 12-100 meshes for the length of the spark channel. The choice to use 40 points was made to properly model both the unstretched and fully stretched spark channel. A smaller number of points may not accurately model the fully stretched spark channel, whereas a large number of points may not accurately model the unstretched spark channel as it led to increased anomalous local wrinkling of the arc.

The diameter of the plasma channel was estimated as on the order of 100 µm based on the literature [27,28,29]. In this particular simulation with minimum mesh size of 50 µm, 0.2 mm spark diameter was used to have the spark channel occupy multiple meshes across the diameter.

The computational time demand of this spark ignition model mainly depends on the time-step of the CFD simulation and the ignition circuit model. The time-step of the ignition circuit model depends on the value of the circuit parameters, i.e. resistance, inductance, and capacitance. For the particular simulation case in this paper, the time-step of the CFD simulation is on the order of micro-second, whereas the time-step of the ignition circuit model is on the order of a nano-second. This means an extra 1000 calculation are required for each core. However, this calculation of ignition circuit model is quite simple compared to the CFD solver which requires iterative calculation. For this 10 ms simulation with about 100,000 cells using 24 cores, the additional time with this spark ignition model compared to standard CONVERGE ignition model is about 10 seconds.

Continuous energy deposition into the cells along the spark column makes the local flow field less perturbed compared to the discrete energy input. Thus, the distributed energy input model shows a better representation of the spark column movement under the presence of crossflow.

High-Pressure Optical Vessel Results

The constant volume combustion vessel was used to investigate the ignition circuit and the spark column behavior with crossflow through the gap. The free stream velocity out of the tube was calculated from the flowrate and the diameter of the tube (4.4 mm). The electrodes were located in the potential core region of the emerging nitrogen jet. However, the actual gas velocity between the gap was higher than the free stream velocity as the electrodes blocked and directed part of the flow. The flow field around the spark plug was simulated using CONVERGE CFD to check the local flow velocity at the center of the gap. Figure 17 shows the result of a simulation with a pressure of 12 bar and 5 m/s free stream velocity. The maximum velocity in the middle of the gap was 7 m/s. Figure 18 shows the local flow velocity in the middle of the gap for various free stream velocities. It was found that the local flow velocity at the center of the gap was 23-26% higher than the free stream velocity and independent of the pressure. Gardiner et al. investigated the relationship between the velocity of the spark and the free stream velocity [12]. They found that the velocity of the leading edge of the arc is about one half of the free stream velocity. The reduced column velocity compared to the local flow velocity was used in the simulations to make the spark column move slower than the local flow.

One important thing to note from Figure 17 is the presence of a recirculation zone along the top surface of the ground electrode. The blunt upstream face of the electrode located perpendicular to the crossflow created this recirculation zone on the leading edge of the ground electrode. This recirculation zone made the column attachment point on the ground electrode move upstream, toward the right in Figure 16, during the spark discharge. This is not a realistic movement of the spark column based on the actual spark column

FIGURE 17 Velocity contours around the spark plug for 12 bar pressure and 5 m/s free stream velocity.

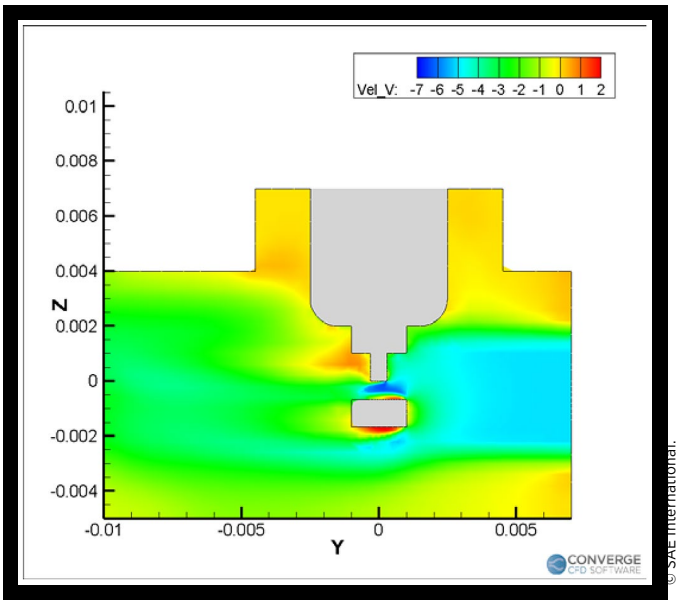

movement captured in the experiments. There are a couple of possibilities to explain this discrepancy of the column movement. The first regards the presence of the recirculation in the experiment. In the simulation, the ground electrode was modeled as rectangular with a flat surface and sharp corners. Also, the electrode was oriented 90 degrees to the crossflow. However, the actual ground electrode may have a rough surface and rounded corners. In addition, the ground electrode may not have been located at a perfect 90 degree angle to the crossflow. These factors will result in a narrowing or absence of the recirculation zone in the actual experiment. The other possibility includes factors affecting the movement of the spark column. We disregarded the actual plasma physics occurring in the spark and arc root attachment zones. We note that our primary interest is the bulk movement of the spark column and the center of the gap where the energy is transferred to the reactive fuel/air mixture.

Figure 19 shows the gap voltage and current profile measured with a crossflow velocity of 5 m/s at 12 bar pressure. Figure 20 shows images of the stretched spark column captured at the same time as the voltage and current. The crossflow direction is from right to left. The center electrode is on the bottom and the ground electrode is on the top. From the voltage profile, it is clear that restrikes occurs at 1.05 and 1.5 ms, coincident with the sudden voltage changes. These events were also captured by the high-speed camera characterized by the short straight column between the two electrodes. The high-speed camera also captured a short-circuit of the spark column at 0.6 ms. A new direct path was formed in the middle of the wrinkled spark column between the two closest points. The voltage also changed slightly with the short-circuit, however, it was not as high as the voltage change with restrike.

FIGURE 18 Local flow velocity vs free flow velocity (left), velocity ratio vs. free stream velocity (right).

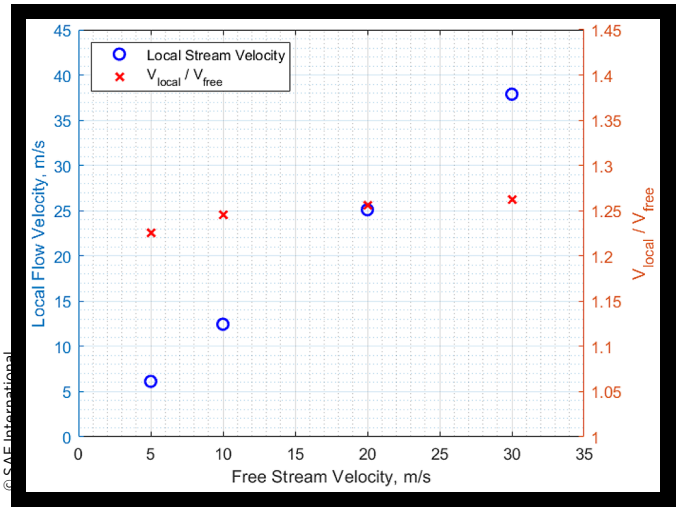

FIGURE 19 Gap voltage and current profiles of the stretched spark column.

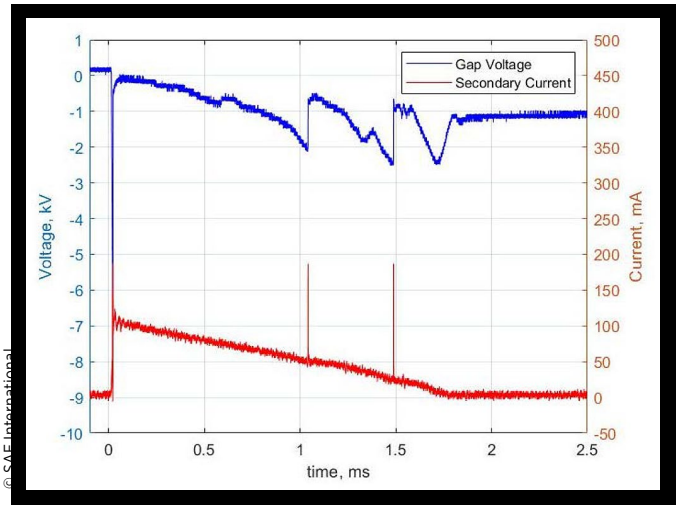

FIGURE 20 Captured images of the stretched spark column.

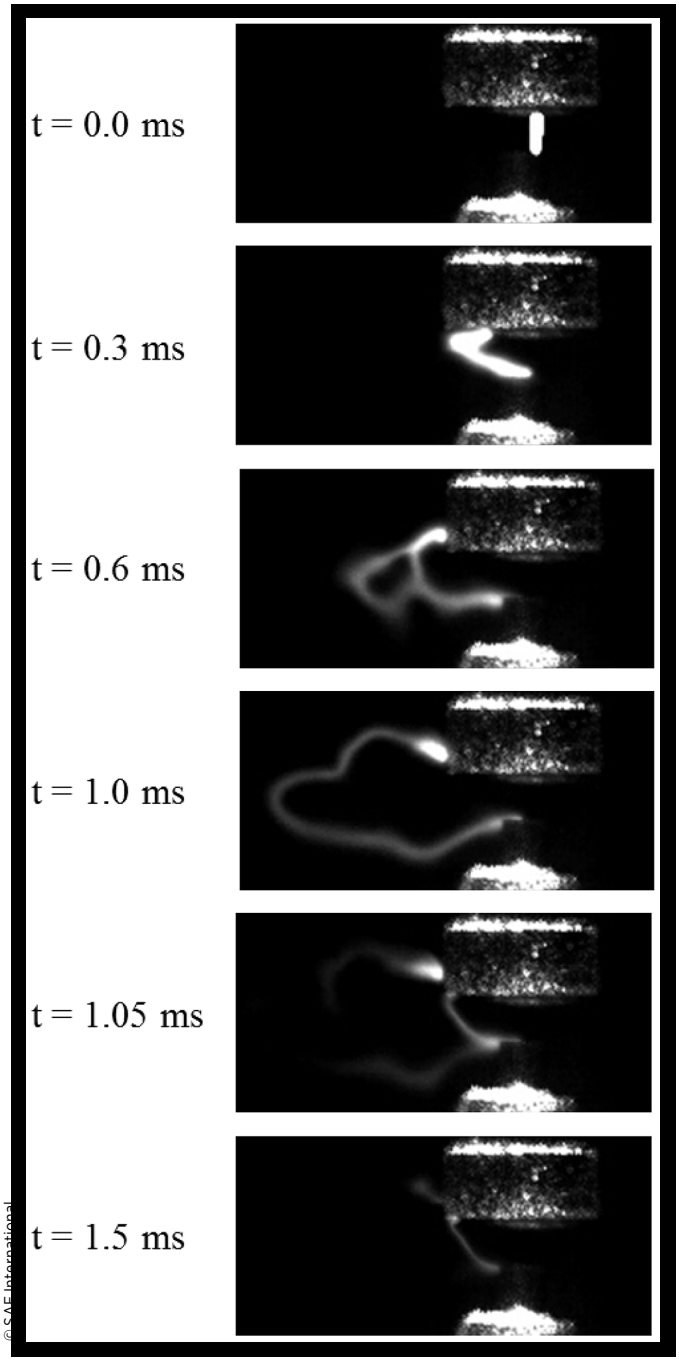

FIGURE 21 Captured images of the stretched spark column at specified times following ignition for a smaller gap of 0.3 mm and for pressures from 6 - 20 bar and crossflow velocities of 5 and 10 m/s.

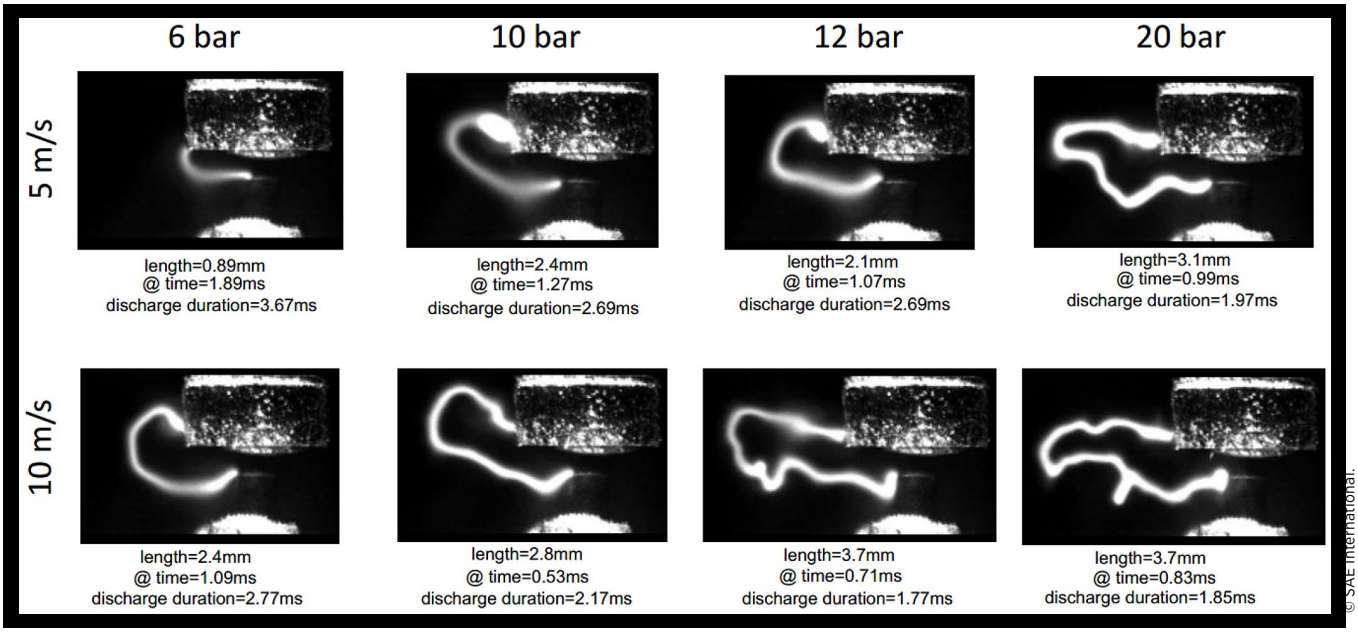

This reveals that short-circuiting may be difficult to identify with the voltage trace alone.

The discharge current is driven by the high inductance of the secondary winding; as a result, the average for the noise component was nearly identical from shot-to-shot for a given set of operating parameters. At the 20 bar pressure condition the arc voltage across the gap was very reproducible near the beginning of the discharge (about -200 volts), but it increased (to a larger negative voltage) as the arc was stretched by the crossflow, which varied from shot-to-shot. In addition, the sudden voltage transitions seen in Figure 19 occur with different frequency and at different times from shot-to shot depending on when the restrikes and short circuits occur.

Figure 21 shows additional examples of the shape of the propagating arc at specific times after ignition obtained under different conditions. The examples in Figure 21 are with a smaller gap of 0.3 mm and for pressures from 6 - 20 bar, and for two cross flow velocities of 5 and 10 m/s. The images provide an impression of the variability of the shape of the stretched arc and its sensitivity to crossflow velocity, gap distance and pressure.

CONVERGE CFD simulations were conducted to simulate the spark column movement with short-circuiting and restrike under the presence of crossflow. As discussed previously, the spark column movement near the surface of the electrodes was not modeled accurately due to the recirculation region in the simulations. Due to this behavior, short-circuiting of the spark column could not be accurately simulated along the arc because of the erroneously large distance between the root attachment points. Only the restrike behavior of the spark column was simulated, done by setting the restrike voltage to the user input value. If the gap voltage exceeded the given restrike voltage anytime during the simulation, a new spark column was formed between the column roots on the two electrodes. If the voltage between any two points along the spark column (eqn. 3) exceeded the short-circuiting voltage (eqn. 4) anytime during the simulation, a new spark column was formed between those points. Figure 22 shows the voltage and current profiles from the simulation. The sudden voltage changes at 1.0 and 1.7 ms indicate that short-circuiting and restrike occurred two times during the 1.8 ms spark discharge. The oscillations in the voltage and current between 0.7 and 1.0 ms and around 1.5 ms originated from instability of the numerical calculation, which can be removed with further development of the ignition circuit model. Figure 23 shows the spark column shape around the times of the short-circuiting and restrike. The stretched spark column is replaced with a new straight spark column in the middle of the spark gap at 1.0 ms. This spark column is again stretched by the crossflow until 1.6 ms when the gap voltage reaches 3.4 kV. Restrike occurred at 1.7 ms with a new straight spark column between the electrodes.

FIGURE 22 Simulation results with spark column movement with restrike.

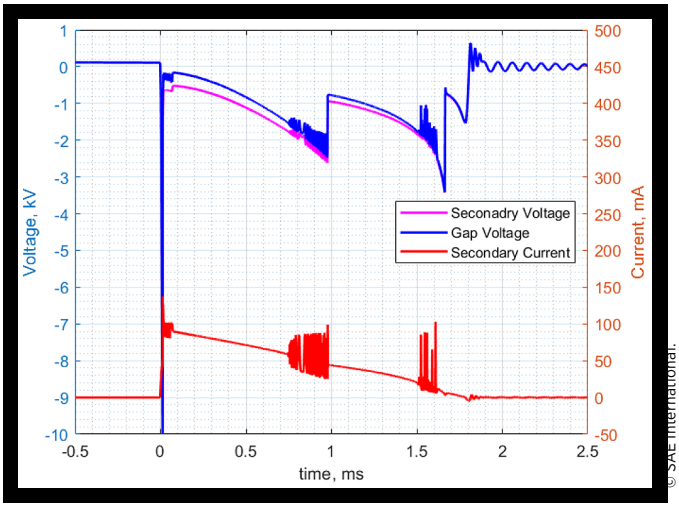

FIGURE 23 Spark column movement simulation with restrike.

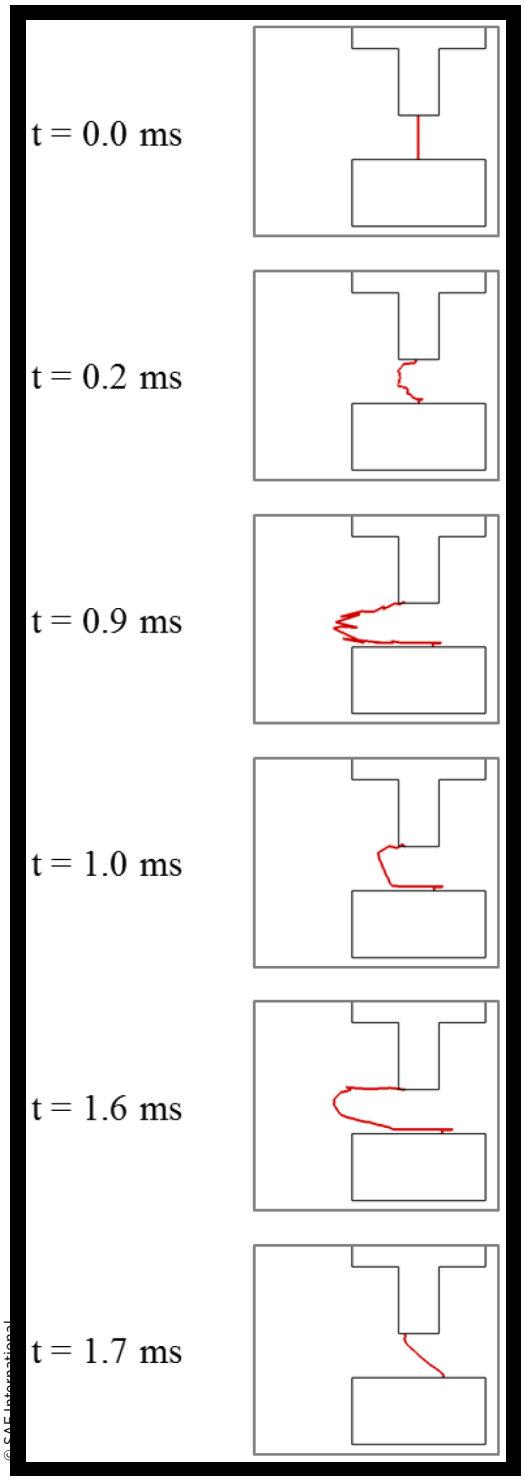

Although the spark column movement near the electrode surface was not well modeled compared to the actual spark column movement, the restrike behavior was simulated well to represent the actual restrike. The CFD simulations with the integrated ignition circuit model made this restrike simulation possible since we can track the gap voltage during the simulation.

At the current stage of development of this model, the channel diameter is set to a fixed value. However, a calculated value from another spark channel model that predicts spark channel growth could be used. The short-circuit or restrike voltage is calculated from the equation (4). It is based on the initial breakdown voltage, spark gap distance, distance between the points of short-circuit/restrike, and a constant C for correlation between the calculation and the measurements. As seen in Figures 19 and 22, the short-circuit or restrike voltage is on the order of 2-3 kV.

Summary/Conclusions

A spark ignition model combined with a transient ignition circuit model was developed and integrated into the CONVERGE™ CFD as a user defined function (UDF) to investigate the transient behavior of spark ignition voltage and current behavior and arc movement and shape. The model incorporates both primary and secondary circuit models that use measured or manufacturer specified parameters. The voltage and current were well simulated for the charging of the coil and for the discharging through the spark column as compared with parameters measured from the experiments. The transient behavior made the thermal energy input to the gas vary during the discharge.

A new distributed energy input model was developed to model how the energy is deposited into the gas within the spark plug gap under the presence of crossflow. The distributed energy input model enabled contiguous energy input to the cells along the spark column and was able to account for the spark column diameter. Compared to the discrete energy input model, the new distributed energy input model showed less perturbation of the spark column movement and a shape more consistent with the experimental imaging of the spark column during crossflow.

The CONVERGE™ CFD simulations integrated with the ignition circuit model, the new distributed energy input model, and the new restrike model were conducted to simulate the spark ignition process under the presence of crossflow. Although the spark column movement results showed some limitations, especially near the surface of the ground electrode due to the presence of a recirculation zone not seen in the experiments, restrike behavior was well captured with the restrike model. This was possible because of the integrated ignition circuit model. Without the integrated ignition circuit model, we would not have been able to evaluate the criterion for restrike.

The current spark ignition model still needs further development, especially with regard to the column movement. Setting the spark column to follow the local flow is not sufficient to model the actual spark column movement from the experiments. Other factors need to be included in this spark column movement model, including electromagnetic self-interaction and a gap resistance model. In addition, the ignition circuit model showed some instabilities during the calculation with restrikes. With further development, an even better representation of the actual spark ignition process in a crossflow environment should be possible.

References

1. Fan, L., Li, G., Han, Z., and Reitz, R., "Modeling Fuel Preparation and Stratified Combustion in a Gasoline Direct Injection Engine," SAE Technical Paper 1999-01-0175, 1999, https://doi.org/10.4271/1999-01-0175.
2. Duclos, J.M. and Colin, O., "Arc and Kernel Tracking Ignition Model for 3D Spark-Ignition Engine Calculations," *Int. Symp. Diagn. Model. Combust. Intern. Combust. Engines* (1):46, 2001.
3. Dahms, R.N., Fansler, T.D., Drake, M.C., Kuo, T.-W. et al., "Modeling Ignition Phenomena in Spray-Guided Spark-Ignited Engines," *Proc. Combust. Inst.* 32:2743-2750, 2009, doi:10.1016/j.proci.2008.05.052.
4. Lucchini, T., Cornolti, L., Montenegro, G., D'Errico, G. et al., "A Comprehensive Model to Predict the Initial Stage of Combustion in SI Engines," SAE Technical Paper 2013-01-1087, 2013, https://doi.org/10.4271/2013-01-1087.
5. Richards, K.J., Senecal, P.K., and Pomraning, E., *CONVERGE Users Guide & Reference Manual (Version 1.4.1)* (Middleton, WI: Convergent Science Ing., 2012).
6. Yang, X., Solomon, A., and Kuo, T., "Ignition and Combustion Simulations of Spray-Guided SIDI Engine using Arrhenius Combustion with Spark-Energy Deposition Model," SAE Technical Paper 2012-01-0147, 2012, https://doi.org/10.4271/2012-01-0147.
7. Scarcelli, R., Zhang, A., Wallner, T., Som, S., Huang, J., Wijeyakulasuriya, S., Mao, Y., Zhu, X., and Lee, S.-Y., "Development of a Hybrid Lagrangian-Eulerian Model to Describe Spark-Ignition Processes at Engine-Like Turbulent Flow Conditions," in *ASME 2018 Internal Combustion Engine Division Fall Technical Conference*, 2018, doi:10.1115/ICEF2018-9690.
8. Sforza, L., Lucchini, T., Onorati, A., Zhu, X. et al., "Modeling Ignition and Premixed Combustion Including Flame Stretch Effects," SAE Technical Paper 2017-01-0553, 2017, https://doi.org/10.4271/2017-01-0553.
9. Masuda, R., Sayama, S., Fuyuto, T., Nagaoka, M. et al., "Application of Models of Short Circuits and Blow-Outs of Spark Channels under High-Velocity Flow Conditions to Spark Ignition Simulation," SAE Technical Paper 2018-01-1727, 2018, https://doi.org/10.4271/2018-01-1727.
10. Mantel, T., "Three Dimensional Study of Flame Kernel Formation Around a Spark Plug," SAE Technical Paper 920587, 1992, https://doi.org/10.4271/920587.
11. Kim, J. and Anderson, R., "Spark Anemometry of Bulk Gas Velocity at the Plug Gap of a Firing Engine," SAE Technical Paper 952459, 1995, https://doi.org/10.4271/952459.
12. Gardiner, D., Wang, G., Bardon, M. et al., "An Experimental Study of Spark Anemometry for In-Cylinder Velocity Measurements," *J. Eng. Gas Turbines Power* 130(4):042801, 2008, doi:10.1115/1.2898835.
13. Stevenson, R., Palma, R., Yang, C., Park, S. et al., "Comprehensive Modeling of Automotive Ignition Systems," SAE Technical Paper 2007-01-1589, 2007, https://doi.org/10.4271/2007-01-1589.
14. Wang, Q., Zheng, Y., Yu, J., and Jia, J., "Circuit Model and Parasitic Parameter Extraction of the Spark Plug in the Ignition System," *Turk J. of Elec. Eng. & Comp. Sci.* 20(5), 2012, doi:10.3906/elk-1009-751.
15. Yu, S., Tan, Q., Ives, M., Liu, M. et al., "Parametric Analysis of Ignition Circuit Components on Spark Discharge Characteristics," SAE Technical Paper 2016-01-1011, 2016, https://doi.org/10.4271/2016-01-1011.
16. Tan, Q., Yu, S., Chen, X., and Zheng, M., "Spark Ignition Circuit Energy Characterization based on a Simplified Model and Measurement Analysis," SAE Technical Paper 2015-01-1271, 2015, https://doi.org/10.4271/2015-01-1271.
17. Roth, W., Guest, P.G., Elbe, G., and Lewis, B., "Heat Generation by Electric Sparks and Rate of Heat Loss to the Spark Electrodes," *Journal of Chemical Physics* 19(12):1530-1535, 1951.
18. Merritt, L.R., "A Spark Calorimeter," *Journal of Physics E: Scientific Instruments* 11:193-194, 1978.
19. Franke, A. and Reinmann, R., "Calorimetric Characterization of Commercial Ignition Systems," SAE Technical Paper 2000-01-0548, 2000, https://doi.org/10.4271/2000-01-0548.
20. Teets, R.E. and Sell, J.A., "Calorimetry of Ignition Sparks," SAE Technical Paper 880204, 1988.
21. Abidin, Z. and Chadwell, C., "Parametric Study and Secondary Circuit Model Calibration Using Spark Calorimeter Testing," SAE Technical Paper 2015-01-0778, 2015, https://doi.org/10.4271/2015-01-0778.
22. Alger, T., Mangold, B., Mehta, D., and Roberts, C., "The Effect of Sparkplug Design on Initial Flame Kernel Development and Sparkplug Performance," SAE Technical Paper 2006-01-0224, 2006, https://doi.org/10.4271/2006-01-0224.
23. Meek, N.F., *Electrical Breakdown of Gases; Oxford at the* (London, UK: Clarendon Press, 1953).
24. Kim, K., Hall, M.J., Wilson, P.S., and Matthews, R.D., "Arc-Phase Spark Plug Energy Deposition Characteristics Measured Using a Spark Plug Calorimeter Based on Differential Pressure Measurement," *Energies* 13:3550, 2020, doi:10.3390/en13143550.
25. Sprunger, Douglas, Private Communication, Cummins, Inc. 2020.
26. Maly, R. and Vogel, M., "Initiation and Propagation of Flame Fronts in Lean CH4-Air Mixtures by the Three Modes of the Ignition Spark," in *17th Symposium on Combustion, the Combustion Institute*, pp. 821-831, 1978.
27. Maly, R.R. and Herweg, R., "Spark Ignition and Combustion in Four-Stroke Gasoline Engines," . In: *Flow and Combustion in Reciprocating Engines*. (Spring Berlin Heidelberg, 2009), 1-66.
28. Sher, E., Ben-Ya'Ish, J., and Vravchik, T., "On the Birth of Spark Channels", *Combust. Flame* 89(2):186-194, 1992, doi:10.1016:/0010-2180(92)90027-M
29. Ishii, K., Tsukamoto, T., Ujiie, Y., and Kono, M., "Analysis of Ignition Mechanism of Combustible Mixtures by Composite Sparks," *Combust. Flame* 91(2):153-164, 1992, doi:10.1016/0010-2180(92)90097-9.

Contact Information

Prof. Matthew J. Hall
mjhall@mail.utexas.edu
The University of Texas at Austin
Department of Mechanical Engineering
204 E. Dean Keeton St. C2200
Austin, TX 78712

Acknowledgments

This project was made possible through the funding provided by Cummins Inc. through the University of Texas at Austin site of the National Science Foundation Center for Efficient Vehicles and Sustainable Transportation Systems (EV-STS). The authors wish to express their gratitude to Cummins Inc. for their financial support of this project.

We wish to thank ConvergeCFD™ for providing us with licenses for their simulation software and for their generous technical support.

Definitions/Abbreviations

AKTIM - Arc and Kernel Tracking Ignition Model
CAD - Crank Angle Degrees
CFD - Computational Fluid Dynamics
DPIK - Discrete Particle Ignition Kernel
FPS - Frames Per Second
IGBT - Insulated Gate Bipolar Transistor
LESI - Lagrangian-Eulerian Spark-Ignition
SparkCIMM - Spark Channel Ignition Monitoring Model
UDF - User Defined Function

ISSN 0148-7191